



Study of shaking table test of seismic subsidence loess landslides induced by the coupling effect of earthquakes and rainfall

Xiaowu Pu^{1,2} · Lanmin Wang^{1,2} · Ping Wang^{1,2} · Shaofeng Chai^{1,2}

Received: 15 May 2019 / Accepted: 25 April 2020 / Published online: 8 May 2020
© Springer Nature B.V. 2020

Abstract

Light rain or moderate rain is the most common meteorological event in the rainy season in the loess area of China, so the probability of landslide hazards induced by the coupling effect of earthquakes and rainfall under the condition of light rain or moderate rain is relatively higher than that under heavy rain. To study the dynamic response characteristics and instability mechanism of loess slopes by the coupling effect of earthquakes and rainfall under the conditions of moderate rain and light rain, a low-angle slope model test of a large-scale shaking table after 10 mm of rainfall was carried out. By gradually increasing the dynamic loading, the evolution of the macroscopic deformation and the instability failure mode of the slope model are observed; the temporal and spatial trends of the amplification effect, acceleration spectrum, pore pressure and soil pressure are analyzed; and the failure mechanism of the slope is determined. The results showed that the amplification effect increased along the slope surface upward, and a strong amplification effect appeared at the front of the top of the slope. Because of the stronger dynamic stress action on the upper part of the slope, the immersed soil in the upper part of the slope experienced seismic subsidence deformation, the saturation in the seismic subsidence soil increased, and the water content temporarily increased locally. With the further increase in the loading intensity, a large number of tension cracks were generated in the seismic subsidence area, and water infiltrated down along the cracks and the wetting range expanded under dynamic action. The range of seismic subsidence and cracks further extended to the deep part of the slope. Under the reciprocating action of the subsequent ground motion, the swing amplitude of the soil mass in the seismic subsidence area, which is divided by a large number of cracks in the upper part of the slope, increased further, resulting in the further reduction in the residual strength of the seismic subsidence soil mass located at the crack tip due to the pull and shear action. Finally, under the combined action of gravity and dynamic force, the upper soil mass in the seismic subsidence area dragged the lower soil mass in the seismic subsidence area downward because the sliding force is greater than the residual strength of the soil mass, which induced a seismic subsidence-type loess landslide. Under the coupling effect of earthquakes and rainfall, the instability mode and mechanism of this landslide are significantly different from those of liquefaction-type landslides.

Keywords Rainfall · Coupling effect · Shaking table model test · Instability mechanism

1 Introduction

Loess is a special variety of soil widely distributed in northern China. Its unique material source, the special environment where it is found and its long-term internal–external geological agent effect together have shaped the macroscopic landforms in the loess area featured by crisscrossed and fragmented gullies. On the microscopic scale, loess is characterized by high porosity and weak cementation, and metastable scaffold pores are extremely well developed. These pores exhibit mechanical collapsibility behavior when they meet water, seismic subsidence when they are subjected to earthquake action (Gao 1994; Wang 2003; Deng et al. 2013) and present strong dynamic catastrophic characteristics. In the events of moderate or strong earthquakes, extremely serious geotechnical disasters can be induced (Zhang 1999).

In recent years, with the progress of the Western Development in China and the Belt and Road Initiative, based on the accumulated capital, science, technology, equipment and intelligence since the reform and opening up, the people of the loess area in China have shifted their mentality from passive environmental adaptation to active large-scale environmental transformation. Various transportation, water conservancy and urban construction projects have been widely implemented, while the urbanization process has been advanced at a high pace. In addition, a large number of high, steep loess slopes have emerged, which have led to a sharp increase in the risk of loess landslides (Wang and Sun 2014).

Landslides are one of the main methods of geomorphological evolution and are also widely developed geological hazards. Their natural inducing factors are mainly rainfall and earthquakes. Generally, the probability of rainfall and earthquakes occurring in the same area is not high; however, sometimes rainfall and earthquakes occur together so that more severe landslide disasters are induced or a landslide occurs in a place where it would not have occurred under the action of a single triggering factor. For example, the 2004 Mid-Niigata Prefecture earthquake (M6.8) caused many large-scale landslides and many landslide dams, and the 2006 Southern Leyte landslide was triggered by a nearby small earthquake (M2.6). The main causes of these landslides are the coupled effects of earthquakes and rainfall (Sassa et al. 2007). Later, through field investigation and ring shear tests, on the basis of an in-depth study of the mechanism of initiation and motion of these landslides and combining the study with previous research results (Sassa et al. 2004), a simulation model, LS-RAPID, was developed (Sassa et al. 2010). In 2018, the Hokkaido Ms6.7 earthquake in Japan induced more than 4000 landslides due to the coupled effect of earthquakes and rainfall. These landslides, induced by the coupling action of earthquakes and rainfall, have common characteristics: longer travel distance and mostly low-angle landslides with slopes ranging from 15° to 30° (Wang et al. 2019a, b). Similar phenomena of landslides induced by the coupling of earthquakes and rainfall also occurred in Indonesia, and the initiation mechanism of earthquake-induced landslides during rainfall was studied (Faris and Fawu 2014). The above-mentioned landslides that occurred in rain-rich areas due to the coupled effects of earthquakes and rainfall have similar mechanisms of initiation. Namely, the rainfall before an earthquake causes the groundwater level to rise, and the soil in the potential sliding zone is saturated. The saturated soil layer is subjected to pore pressure generation and liquefaction during seismic shaking and postfailure shear displacement. Subsequently, under the action of seismic force and gravity, sudden, fast and long-distance sliding of the sliding zone soil layer and the overlying nonliquefied soil layer occurs (Sassa et al. 2007, 2010; Faris and Fawu 2014).

Since the occurrence of mud-like loess landslide disasters in Yongguang Village during the Minzhang Ms6.6 Earthquake in Gansu, China, loess landslides induced by the coupling effect of earthquakes and rainfall have received widespread attention from the geotechnical engineering community. Many experts have carried out relevant research work, and the characteristics and inducing causes were analyzed through detailed field investigation (Xu et al. 2013; Wang et al. 2019a, b). The liquefaction probability of the loess was indicated through dynamic triaxial liquefaction tests, and the disaster-causing mechanism of the Yongguang landslide was revealed by numerical simulation (Wu et al. 2019). The above-mentioned research results on the Yongguang landslide indicate that the landslide was caused by liquefaction and sliding of the soil mass of the slope surface due to the coupling of earthquakes and rainfall. However, these conclusions are reasonably deduced based on site investigation, triaxial tests and numerical analysis. Because the shaking table test could visually reproduce the process of slope failure, the loess slope failure tests under the coupling of earthquakes and rainfall have also been implemented. The results show that the PGA (peak ground acceleration) magnification effect of the slope is stronger after heavy rainfall (Wang et al. 2017a, b), and the loess at the slope top would liquefy and slide along the slope under the action of seismic ground motion. In addition, the results show that regardless of macroscopic phenomena or pore pressure, soil pressure and acceleration time history, significant liquefaction phenomena of the loess could be observed (Wang et al. 2018).

From the above-mentioned research results at home and abroad, it can be seen that there is a process of heavy rainfall or long-term rainfall before the landslides induced by the coupling of earthquakes and rainfall, and the landslides are basically caused by liquefaction and slip of the soil mass. However, the loess area in China is mostly distributed in arid and semiarid areas, which are characterized by little but concentrated rainfall, moderate or small rains, and heavy rains of short duration. Therefore, under these conditions, the probability of loess landslides induced by the coupling effect of earthquakes and rainfall is higher, which is a scientific problem that needs to be further studied. However, under such rainfall conditions, are loess landslides induced by the coupling of earthquakes and rainfall necessarily caused by the liquefaction and slip of the soil mass? Are there any other slope failure modes and mechanisms? In 1995, massive loess landslides were induced by the Yongdeng Ms5.8 earthquake in Gansu Province, China. The postearthquake investigation and experimental analysis indicated that the short-duration heavy rains before the earthquakes increased the water content in the loess slope, and the earthquake caused the loess subsidence of the slope surface, thereby inducing many seismic subsidence loess landslides (Qi et al. 1998). The infiltration range of medium and small rains in the loess slopes is similar to that of the short-duration heavy rain, which only increases the soil water content in the limited range of the slope surface (Zhang et al. 2014). To reveal the failure mode and mechanism of loess slopes induced by the coupling effect of earthquakes and rainfall under medium and small rain conditions and then propose the evaluation method of slope stability, a low-angle loess slope was selected as the research object, and a shaking table was selected as the main test means. The shaking table model test of loess slopes was carried out under 10-mm rainfall conditions. The results of this study lay a scientific research foundation for landslide risk prevention and control, engineering prevention and disaster relief.

2 Test conditions

To facilitate the comparative analysis of the loess landslides in the Yongdeng earthquake, through a field survey we selected a typical Q_3 loess slope with a height of 7 m and an angle of 20° , both of which are commonly found in the Lanzhou New District, and implemented extensive engineering construction to establish a generalized model. The Lanzhou New Area is adjacent to Yongdeng, and the two places are similar in topography and geomorphology. The reason for choosing a low-angle low slope is that the original slope gradient of a large number of earthquake-induced loess landslides is 10° – 30° (Chen and Shi 2006; Deng and Fan 2013). These low slopes are usually very stable, and their disaster prevention problems are more easily ignored by people.

2.1 Test equipment

A large two-direction electric servo shaking table from Lanzhou Institute of Seismology of China Earthquake Administration is used as the shaking equipment (Fig. 1). The table size is $4\text{ m} \times 6\text{ m}$, the frequency range is 0.1–70 Hz, and the maximum acceleration is 1.7 g. In the test, a rigid model box with a size of $2.82\text{ m} \times 1.42\text{ m} \times 1.1\text{ m}$ is adopted, which is made of a carbon steel plate while the long edges are made of organic glass plates.

2.2 Similarity relationship and material parameters

The key to the model test is to reproduce the deformation instability and failure process of the loess slope. Therefore, the similarity of resistance is mainly considered to ensure the similarity of the deformation and failure behavior between the prototype and the model (Lin et al. 2000). Therefore, the similarity ratios for geometrical size, cohesion and density are determined as the main control parameters, and the similarity relationships are shown in Table 1. To ensure a certain degree of similarity of the loess microstructure, the remolded loess of the prototype site was used to make the model, and the soil material parameters are shown in Table 2.

Fig. 1 Large-scale shaking table



Table 1 Similarity relationships

Physical parameters	Similarity relationship	Similarity ratio	Remark
Geometrical size (L)	$C_L = 10$	10	Control parameter
Density (ρ)	$C_\rho = 1$	1	Control parameter
Acceleration (a)	$C_a = 1$	1	Control parameter
Cohesion (c)	$C_c = C_L C_\rho$	10	
Inner friction angle (φ)	$C_\varphi = 1$	1	
Elastic modulus (E)	$C_E = C_L C_\rho$	10	
Poisson's ratio	$C_\mu = 1$	1	
Time (t)	$C_t = \sqrt{C_L}$	3.16	

Table 2 Soil material parameters

Physical parameters	Similarity constant	Actual value of prototype soil	Target value of model soil	Test value of model soil
Water content (%)	1	4.1–6.5	4.1–6.5	6
Density (10^3 kg/m^3)	1	1.21–1.42	1.21–1.43	1.32
Cohesion (kPa)	10	26–41	2.6–4.1	3.2
Internal friction angle ($^\circ$)	1	21–33	21–33	26

2.3 Loading of earthquake waves

A large number of loess seismic landslides occur mostly in areas with seismic intensities of VIII degrees or above under the action of a strong earthquake (Zhang 1999), and slope failure is generally believed to be caused by horizontal shear waves. Therefore, the NS-direction acceleration time history record (Fig. 2) measured at the Minxian seismic station during the Ms6.6 Minzhang earthquake on July 22, 2013, was selected in the test. The PGA of the seismic wave is approximately 220 gal (VIII degrees), which is the near-field wave recorded by the bedrock base, and the predominant frequency is 4.2 Hz. The loading amplitude is increased step by step until the model is unstable.

2.4 Model making and sensor layout

To reduce the shaking boundary effect, 3-cm-thick plastic foam boards were placed inside the front and rear (shaking direction) steel plates of the model box.

The undisturbed loess was crushed and sieved and compacted every 10 cm. A total of 15 accelerometers, A1 to E5, were arranged. There were 6 pore pressure sensors K1 to K6 and 6 soil pressure sensors YB1–YB6 on the surface of the slope. The model size and sensor position are shown in Fig. 3.

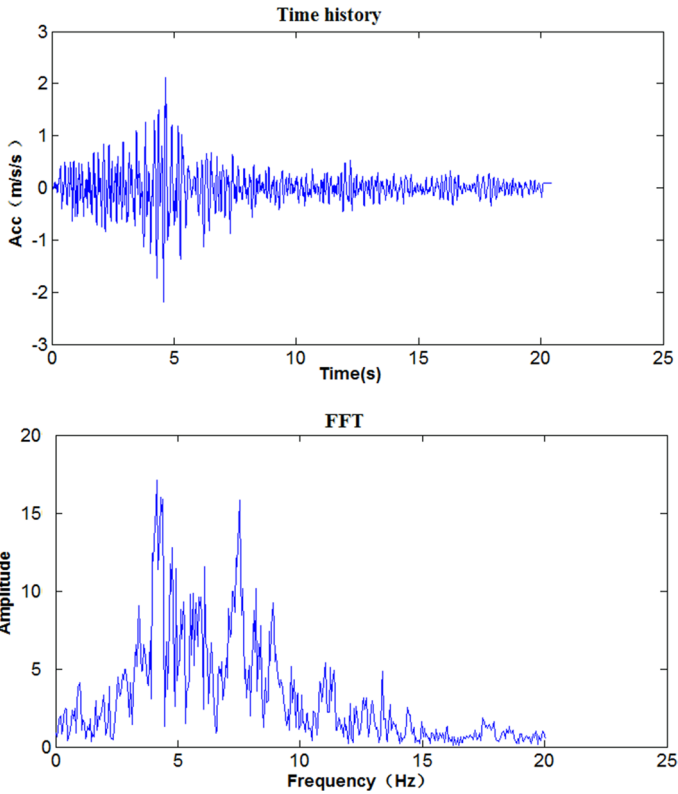


Fig. 2 Time history and Fourier spectrum of the Minxian-Zhangxian seismic wave

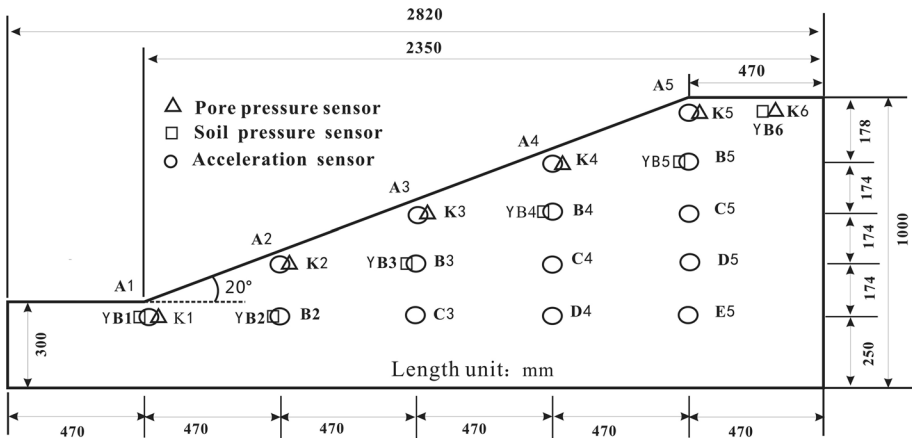


Fig. 3 Model size and sensor layout location

2.5 Rainfall implementation

After the model was completed, artificial rainfall at a rate of 10 mm/h and a total rainfall of 10 mm were simulated by a homemade rainfall device. After the rain, the water content of the rain-soaked soil varied from 21 to 17% within 5–6 cm of the surface layer, and there is a sharp gradient change zone of the water content from 17 to 7% within the 0.5 cm range of the permeability front (Fig. 16a).

The rainfall penetration process on the slope is very complicated. According to the rainfall penetration model of Mein–Larson (Mein and Larson 1973), rainfall penetration is controlled by the rainfall intensity, permeability coefficient and allowable penetration volume control. Due to the complexity of the above rainfall penetration process, the similarity of the rainfall in this test is not strictly considered. However, the comparison between the infiltration results of the artificial rainfall and the field monitoring results (Zhang et al. 2014) shows that the rainfall in the model test is equivalent to the magnitude of a moderate rain to light rain. Thus, the rainfall in the model is in line with our test purpose.

3 Macroscopic deformation evolution and failure modes of the model

The model slope showed no obvious soil damage under the action of 64 gal and 125 gal ground motions.

Under the action of 232 gal ground motion, a slight residual deformation of approximately 5 mm appeared in the shoulder area.

Under the action of 435 gal ground motion, the soil at the slope top was seriously damaged, soil seismic subsidence occurred in the surface area above 1/2 of the slope surface, the seismic subsidence increased gradually from the lower part to the top of the slope, and the seismic subsidence at the top of the slope was approximately 2 cm. The slope shoulder soil slid downward due to the seismic subsidence, and the saturation of the soil mass increased due to compaction. The water at the front edge of the slope shoulder leached out, exhibiting liquefaction-like characteristics. Several tensile cracks appeared in the surface area above 1/2 of the slope surface and the slope top, with a maximum opening of approximately 1–2 cm and a maximum depth of 10 cm. Because of the seismic subsidence of the soil mass, the temporarily increased water content permeated down with the cracks, which spread the wetting range deeper into the soil. The above macroscopic characteristics indicate local instability failure in the slope model.

As seen from Fig. 4, under the action of 647 gal ground motion, the seismic subsidence of the slope top was aggravated, the cumulative maximum seismic subsidence was up to 5 cm, and the cracks extended to 25 cm deep. The slope shoulder and the lower edge soil mass slid downward, the surface sliding amount was approximately 5–7 cm, and the deep sliding amount was approximately 1–2 cm, showing a decreasing trend of the sliding amount from the surface to the inside. The soil mass from the 1/2 slope surface to the slope shoulder experienced both vertical seismic subsidence and downward sliding along the slope, and both the seismic subsidence and the sliding amount decreased with decreasing height. The failure characteristics of the shaking table model were very similar to those of the loess slope failure induced by the Yongdeng Ms5.8 earthquake in 1995 (Fig. 4a, b). The earthquake intensity of the Yongdeng earthquake was VIII. Considering that the amplification effect of the loess slope will increase the



(a) Gedi beam damage of the 1995 Yongdeng Ms5.8 earthquake in Gansu province test

(b) Macroscopic failure phenomenon in the shaking table model

Fig. 4 Macroscopic deformation and failure of the loess slope under the coupling action of earthquake and rainfall

ground motion response of the slope top, it is estimated that the ground motion of the loess ridge top will reach 400–600 gal. Thus, the results of the shaking table test are basically consistent with the loess landslides in the Yongdeng earthquake.

4 Dynamic response characteristics of the model

In the shaking table model test, the dynamic response characteristics of the loess slope from deformation to instability failure can be investigated by increasing the ground motion intensity step by step.

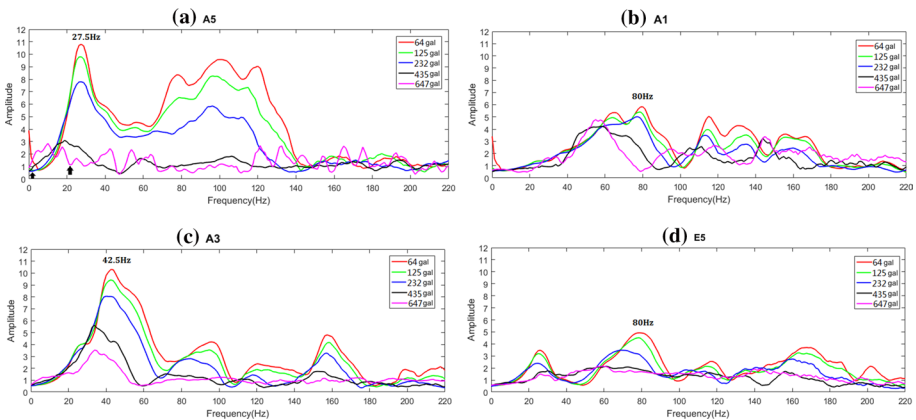


Fig. 5 Spectrum curves of the transfer functions of the slope at locations A1, A3, A5 and E5

4.1 Temporal–spatial evolution of the self-vibration characteristics of the model

Four points at different parts of the model slope, namely A1 (slope foot), A3 (slope middle), A5 (slope shoulder) and E5 (inside the slope), were selected to study the evolution of the self-vibration characteristics of the slope model by the transfer function spectrum (TFS) curve (Jiang et al. 2010). As shown in Fig. 5, each peak in the curve corresponds to a vibration mode Φ_i , and the corresponding frequency f_i is the natural frequency of the i -order mode. The TFS curve is basically asymmetrically parabolic but differs in height and width; a “higher curve” indicates that the amplification effect of the vibration mode is stronger, and a “wider curve” indicates that the amplification band of the vibration mode is wider.

4.1.1 Spatial variation in the self-vibration characteristics of the model

Figure 6 shows significant differences in the vibration characteristics from the slope foot (A1), the slope middle (A3), the slope top (A5), the outside of the slope (A1) to the inside

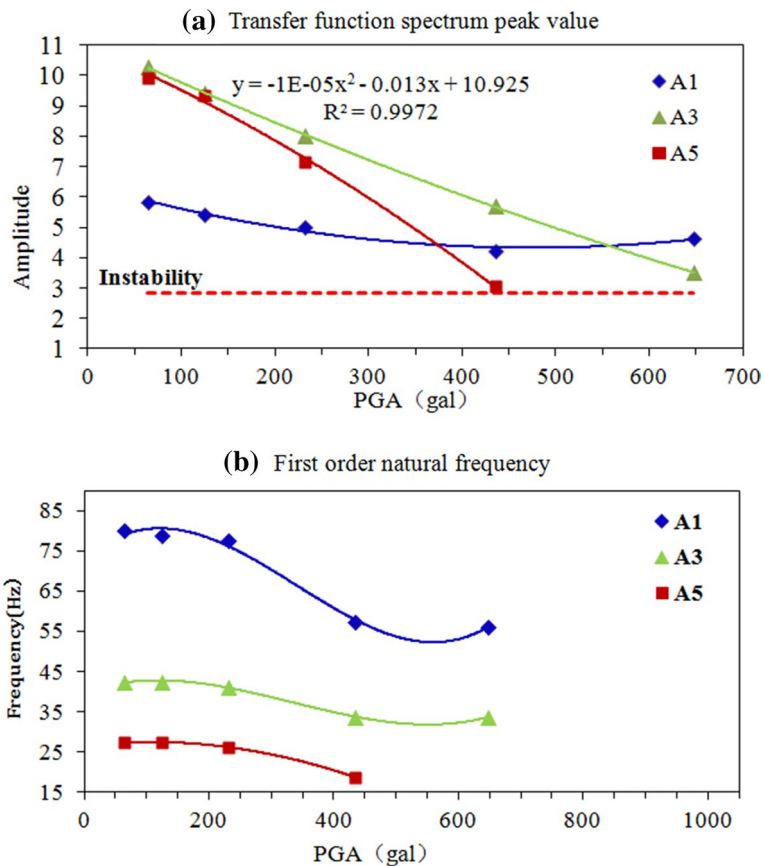


Fig. 6 Peak value of the transfer function spectrum curve at A5 and variation in the model natural frequency

of the slope (E5), which depend on the spatial positions. The lower part of the slope (A1 and E5) contains many vibrational modes, but the response amplitude of the modes is low. As the elevation increases, the vibration modes gradually decrease, but the response amplitude of the modes increases; the natural frequency f_1 of the first-order mode decreases as the elevation increases. For example, the natural frequency f_1 of A1 and E5 are 80 Hz, the natural frequency f_1 of A3 is 42.5 Hz, and the natural frequency f_1 at the slope top is reduced to 27.5 Hz.

4.1.2 Temporal evolution of the self-vibration characteristics of the model

As the dynamic loading intensity increases, the first-order natural frequency at different parts of the model gradually decreases to low frequency, the amplification frequency band becomes narrower, and the amplitude decreases (Figs. 5, 6). The vibration modes of each order are changed to different degrees. In the 435 gal case, the vibration mode of the slope model changes significantly. The second- and higher-order modes at the upper and middle parts of the slope (A3 and A5) disappear. The natural frequency of the first-order mode at A5 is 18.75 Hz, and the response amplitude decreases greatly, indicating local instability on the upper part of the slope. In the 647 gal case, the first-order mode can only be distinguished at A1 and A3 in the middle and lower parts of the slope, while the higher-order modes disappear. The TFS curve at A5 on the slope shoulder shows no obvious peak, and the mean of the amplitude is within 2, which shows instability failure of the slope model (Wang et al. 2017a).

4.2 Spectral response characteristics

The dynamic response of a particular vibration system consists of steady-state response and transient response; the magnitude of the steady-state response is determined by the magnitude of the dominant frequency component in the input wave, while the transient response is the result of the amplified spectral component with the same frequency as the structural natural frequency or the adjacent input wave.

The soil properties at A1, A3 and A5 of the slope are basically the same with initial natural frequencies (64 gal) of 80 Hz, 42.5 Hz and 27.5 Hz, respectively. The main frequency band of the input wave is between 4 Hz and 8 Hz. As the elevation increases, the main frequency of the input wave is closer to the natural frequency of different parts of the slope. Therefore, the dynamic response (steady-state and transient) at A5 at the slope shoulder is significantly stronger than that at A3 and A1 (Fig. 7). As the loading intensity increases, the high-frequency transient response of the slope shoulder decreases (15–30 Hz), the soil damage becomes greater, the frequency band of the high-frequency transient response gradually moves to the low frequency, and the amplitude decreases. In contrast, the low-frequency steady-state response increases as the dynamic loading intensity increases. As the elevation decreases, with the spatial position being different, the high-frequency transient response becomes weaker, and the steady-state response becomes stronger.

4.3 PGA amplification effect

Multiple earthquake cases show that the earthquake motion amplification effect of the loess plays the main role in aggravating disasters (Wu et al. 2012; Wang et al. 2017b). Figures 8 and 9 show that as the slope elevation increases, the PGA amplification coefficient

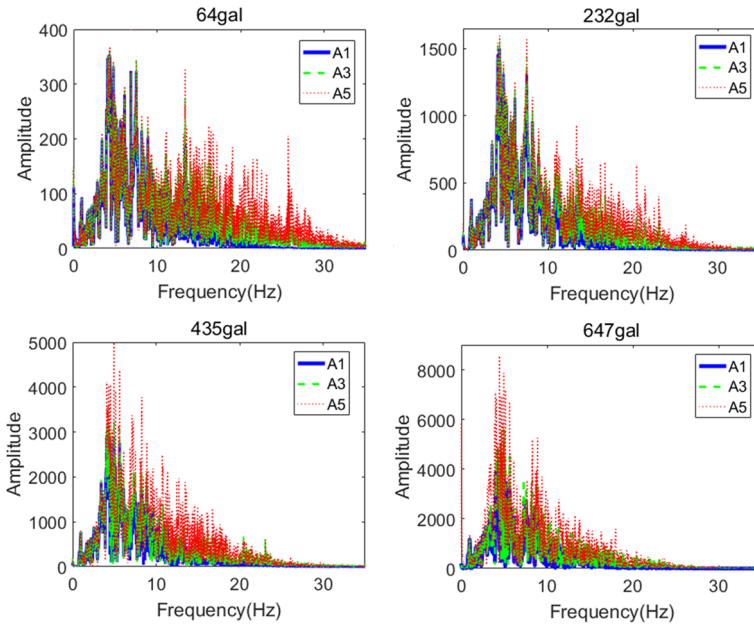


Fig. 7 Fourier spectrum variation in the slope surface acceleration

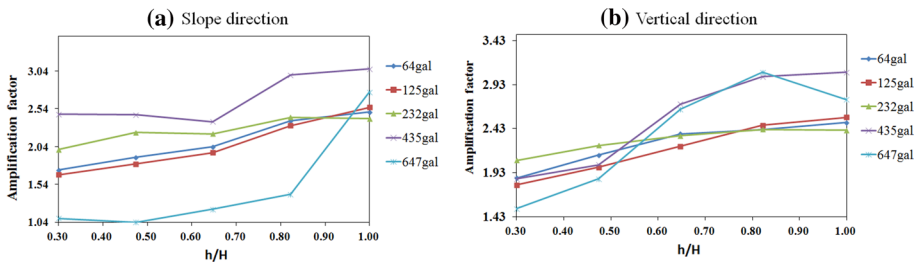


Fig. 8 Variation in the PGA amplification coefficient

increases, presenting strong terrain and elevation amplification effects. These effects are the most significant at the slope top. As the loading intensity increases, the PGA amplification effect is significantly enhanced. The PGA amplification effect in the 435 gal case along the slope is the most significant, and the PGA amplification coefficient of the slope top is 3.07. However, in the 647 gal case, the strong earthquake motion severely damages the soil at the slope surface and the slope top and results in widespread cracks, which abruptly reduces the PGA amplification effect.

4.4 Temporal–spatial evolution of the soil pressure and pore pressure

To compare the dynamic change information, the initial soil pressure and pore pressure are set to zero before loading. Therefore, the measured soil pressure is the total dynamic stress

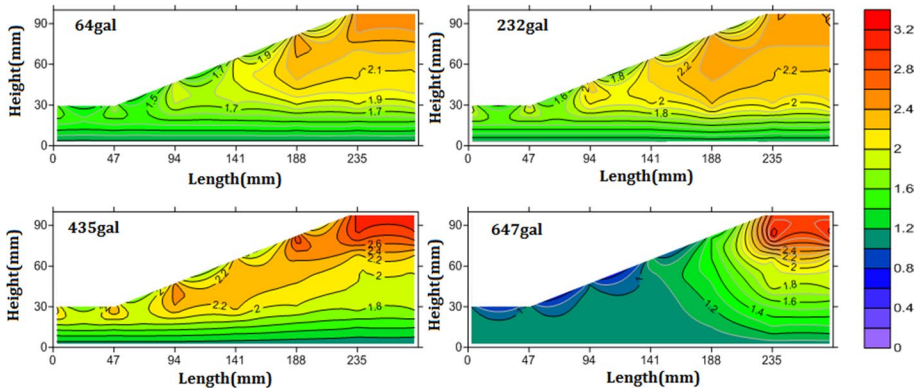


Fig. 9 PGA magnification coefficient nephogram

in the horizontal direction. Positive means compressive, while negative means tensile (relatively tensile and absolute tensile states when exceeding the static lateral pressure). The measured pore pressure is the total dynamic pore pressure in the soil. It is the dynamic water pressure when the soil is saturated; if the soil is unsaturated in the presence of a free water body, the measured pore pressure contains both the dynamic water pressure and the dynamic air pressure. In the absence of a free water body, the measured pore pressure is the dynamic air pressure in the soil, which, however, will not be obvious under dynamic information changes in low loading cases.

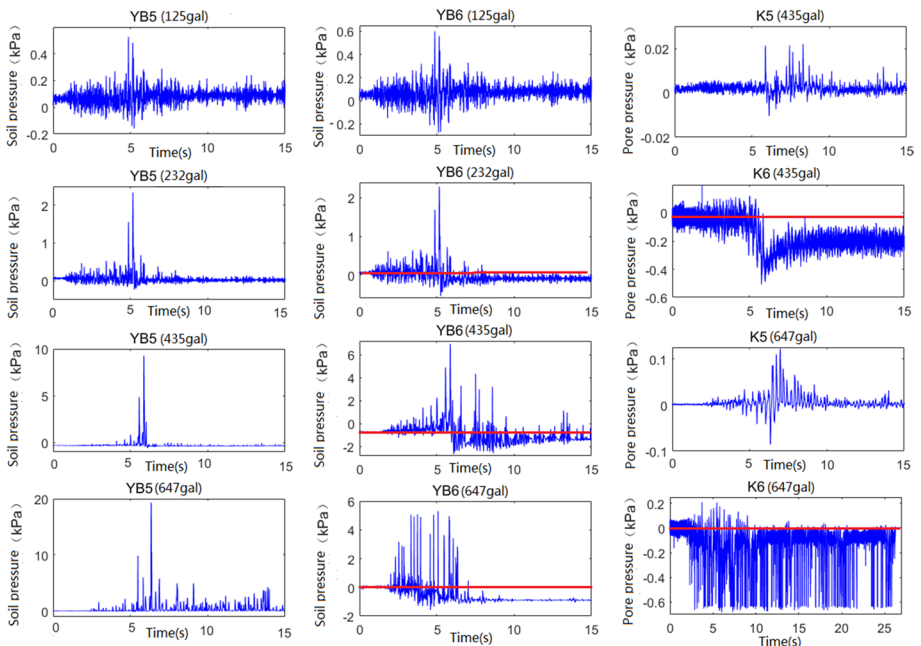


Fig. 10 Time history variation in soil pressure and pore pressure on the slope top

As shown in Fig. 10, in the 125 gal case, the soil pressure at YB5 at the slope shoulder and YB6 at the middle of the slope top fluctuates and is dominated by compressive stress. In the 232 gal case, the compressive stress at the two points is very high, but the tensile stress is very low. In addition, YB6 also exhibits a 0.1 kPa permanent tensile state, which indicates that the soil with a certain damage level cannot effectively transmit the tensile stress action. In addition, the tensile cracks at the slope top reduce the lateral compressive stress on both sides of the cracks, leading to a permanent relative tensile state. In the 435 gal case, the compressive stress at YB5 at the slope shoulder is significantly higher than that at YB6 in the slope, but the tensile stress is low. In addition, YB6 exhibits a strong tensile effect. In addition, the maximum tensile stress is 2.65 kPa, and the absolute tensile stress is 1.25 kPa (the static compressive stress is approximately 1.4 kPa), which exceeds the static lateral compressive stress and results in the absolute tensile stress. Therefore, the soil is subjected to tensile failure, and the permanent tensile stress is 1.33 kPa after the earthquake motion. In the 647 gal case, the changes in the soil pressure at the slope top are similar to those of the previous case, but stronger compressive stress occurs in the slope shoulder where the displacement occurs. The repeated compressive stress at YB6 leads to a small permanent tensile state, which indicates that the soil near the sensor has a void due to tensioning.

After light rain, the maximum saturation at the slope top is approximately 50%, which means that the soil is still unsaturated. The water in the soil basically exists in the pore space in the form of strong–weak combined water or capillary water. In addition, there is no free continuous water body. Therefore, the low dynamic loading case shows no obvious fluctuation in pore pressure, indicating that there is neither water pressure fluctuation caused by free water flow in the pore pressure sensor nor pressure fluctuation caused by gas flow. In the 435 gal case, the pore pressure at K5 at the slope shoulder fluctuates, indicating that the pore space is reduced due to the soil subsidence. As the soil becomes more saturated, a free continuous water body appears locally, while variation in the negative pore pressure appears at K6, which indicates the existence of a negative pressure field after the tensile failure of the soil. In addition, the air permeability of the soil is very poor, and the air pressure inside and outside the soil is isolated. As a result, the soil is still in the negative air pressure state after ground motion. In the 647 gal case, the pore pressure at K5 at the slope shoulder fluctuates in the initial ground motion stage. After the strongest ground motion, the compressive change pattern becomes dominant. At the beginning of the ground motion, a significant variation dominated by negative pressure appears at K6, which reflects the large fluctuation in the pore pressure field in the soil with ground motion.

Due to the seismic subsidence and sliding compaction of the soil at the slope shoulder, no permanent tension is observed in the pore pressure (mainly water pressure) or soil pressure. Tensile cracks appear in the middle of the slope top due to tensile failure; the moisture content penetrates deep, while the pore pressure (air pressure) and soil pressure show permanent tensile changes (the time-history curve deviates from the baseline position).

From the pore pressure spectrum curve in Fig. 11, we can see that the main frequency bands of pore pressure in K5 and K6 are always in line with the input seismic waves, which indicates that the fluctuation in the pore pressure is entirely caused by the seismic waves.

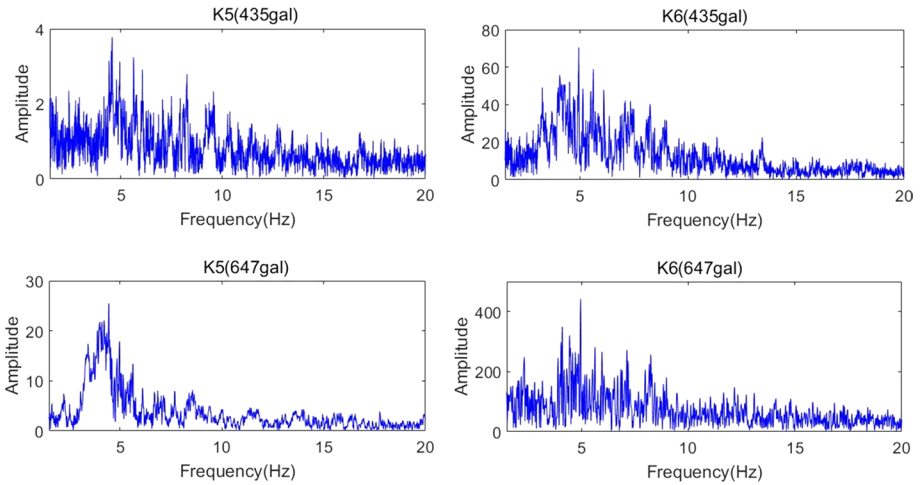


Fig. 11 Fourier spectrum of pore pressure at the slope top

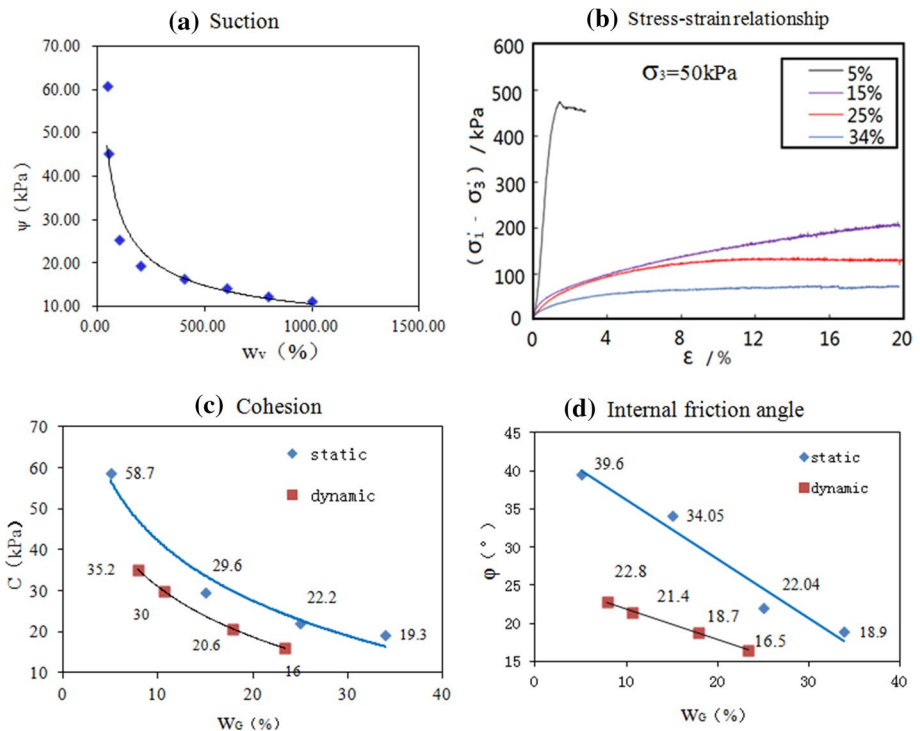


Fig. 12 Changes in the mechanical properties of loess with water content

5 Discussion of the slope instability mechanism induced by the coupled effect of earthquake and rainfall

Based on the results of the shaking table test and other laboratory tests, the mechanism of instability and sliding of seismic subsidence loess landslides after light rain is discussed.

5.1 Changes in the mechanical properties of loess with different water contents

Soil immersed in rainwater will have a great decrease in matrix suction (Fig. 12a). The soil–water characteristic curve of loess can be fitted by the following formula (Yuan et al. 2012):

$$w_v = \frac{1}{a + b \ln(\psi)} \quad (1)$$

where w_v is the volumetric water content, ψ is the matrix suction, and a and b are fitting coefficients. In water-soaked loess, the matrix suction decreases, and the change in the matrix suction will cause a change in the mechanical properties of the loess.

To study the variation in the mechanical properties of loess with water content, several loess samples were collected 5 meters below the top of a slope in the Lanzhou New District, and their dynamic and static strength parameters and stress–strain curves under different water contents were tested. On the whole, the mechanical intensity of the moisturized soil would be reduced. The reduction in dynamic strength will be greater (Fig. 12c, d). The cohesion decreases logarithmically with increasing water content as follows:

$$C_s = -21.13 \ln(w_m) + 90.881 \quad (2)$$

$$C_d = -17.73 \ln(w_m) + 71.842 \quad (3)$$

where C_s and C_d are the static and dynamic cohesion, respectively, and w_m is the mass water content. The internal friction angle decreases linearly with the change in water content as follows:

$$\varphi_s = -0.769w_m + 43.816 \quad (4)$$

$$\varphi_d = -0.3983w_m + 25.805 \quad (5)$$

where φ_s and φ_d are the static and dynamic internal friction angles, respectively. As shown in Fig. 12b, the stress–strain relationship of the loess varies greatly with the water content. The natural state (dry soil) is softening, and brittle failure will occur at low strain (2–3%) (Wang 2003). With increasing water content, the stress–strain relationship is strengthened or ideal elastic–plastic, and the main failure mode is plastic flow failure.

It can be seen from the variation in the mechanical parameters of the loess with the action of water and force that the loess is easily destroyed under the coupling action of dynamic force and water. What are the intrinsic causes of collapsibility and dynamic vulnerability of loess? From the grain size distribution curve and the SEM image of the loess in this area (Figs. 13, 14), we can see that the diameter of the loess particles is mainly distributed between 30 and 70 μm . In the process of aeolian deposition,

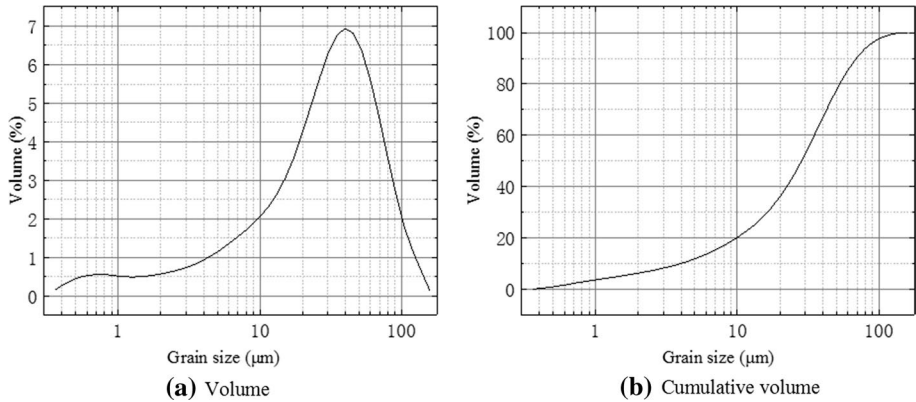


Fig. 13 Loess grain size distribution curve in the Lanzhou New District

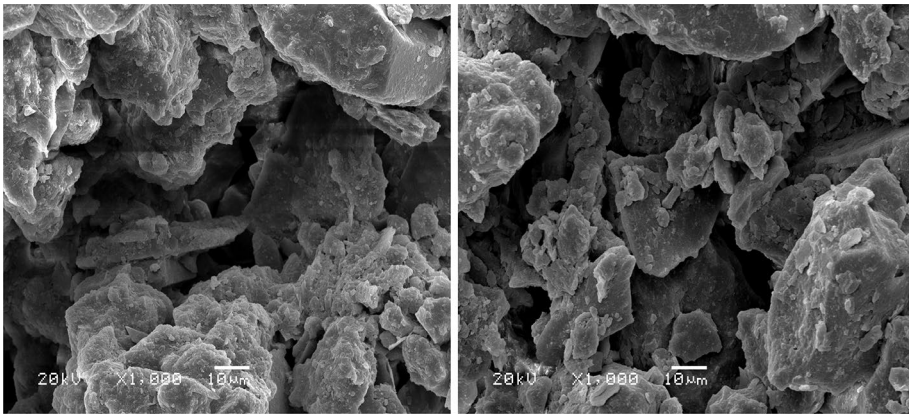


Fig. 14 SEM image of loess in the Lanzhou New District

these medium and large particles with edges and corners support each other and form the macroporous structure of scaffolds under the condition of undercompaction on the surface of the earth. When the loess is soaked, the dissolution of some soluble salts decreases the soil cohesion, while the thickening of the water membrane reduces the internal friction angle. Therefore, the macroporous structure of loess is easily destroyed under small dynamic stress.

5.2 Deformation evolution and failure mechanism of slopes under dynamic loading

The mechanical properties of loess affect the dynamic response characteristics of loess slopes composed of thousands of loess particles. However, the dynamic response, deformation and failure of different parts of the loess slope have their own characteristics due to the stress state and humidity difference. There are four stages in the process of deformation and instability under dynamic loading.

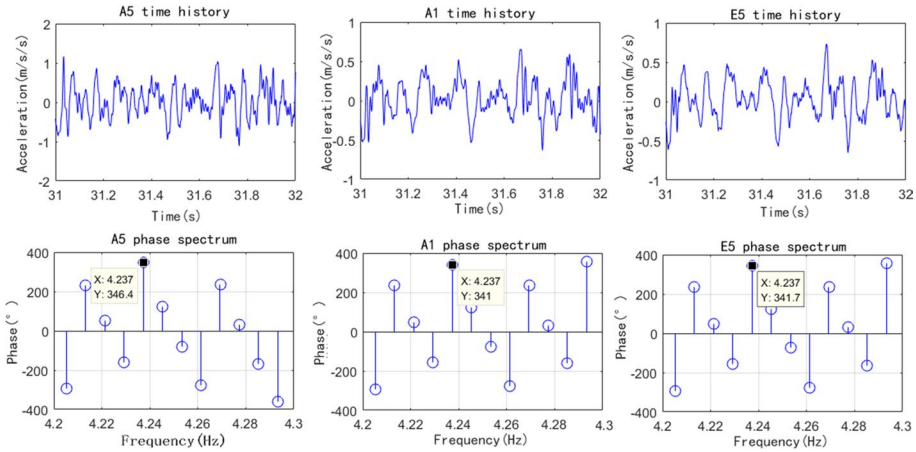


Fig. 15 Acceleration amplitude and phase changes in different parts of the slope (PGA neighborhood)

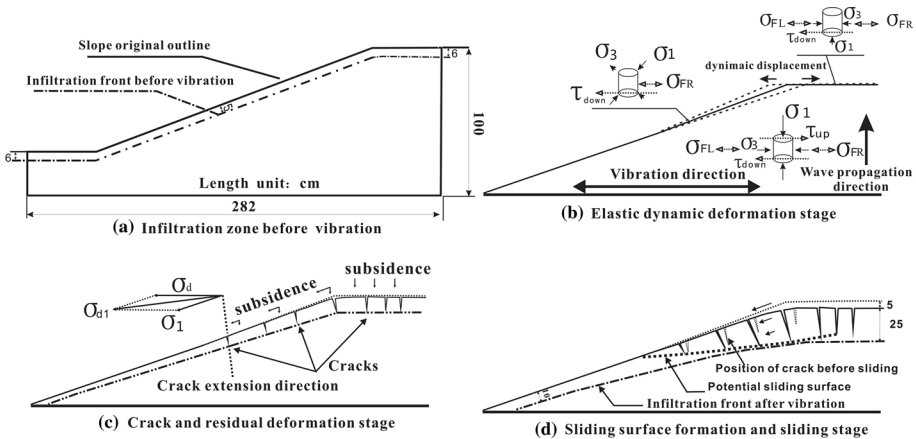


Fig. 16 Schematic diagram of stress and instability failure of the slope

5.2.1 Static force action stage after rainfall

After a light rain, the self-weight of the wetted loess increases and its strength decreases, which leads to an increase in the downward sliding force and a decrease in the anti-sliding force. The moisture content of the wetted soil in certain parts of the loess slope increases, but the soil saturation in the penetration front is between 30 and 50%, which makes it “doubly opened” or “water-closed” unsaturated soil (Luan et al. 2006). Under the condition of the water content, the strength parameters of the soil are still relatively high, the anti-sliding force of the slope is greater than the sliding force, and the slope is in a stable state. The adaptive adjustment of the multiphase soil components in the process of water and gas permeation and migration cannot change the basic structure of the solid skeleton system. Therefore, either the mesoscale of the soil unit or the macroscale of the whole slope does not exhibit deformation.

5.2.2 Dynamic elastic deformation stage

Different parts of the slope after rainfall have different vibration characteristics due to the difference in their mechanical properties and their locations. The amplitude, spectral components and phase of response acceleration in different parts are also significantly different (Fig. 15). Therefore, when the earthquake wave is transmitted from the bottom to the top in the form of stress waves, the soil elements in the slope are subjected to strong dynamic shear stress on the top and bottom sides and to the tensile (compressive) stress from adjacent soil elements on the left and right sides (Fig. 16b). Under seismic ground motion, the dynamic stress of the soil elements in the slope is expressed as follows:

$$(\tau_{\text{down}} - \tau_{\text{up}}) - (\sigma_{\text{FL}} - \sigma_{\text{FR}}) = \rho \left(\frac{\partial^2 u}{\partial t^2} + \frac{\partial^2 u_g}{\partial t^2} \right) \tag{6}$$

where τ_{down} and τ_{up} are the shear stresses of the upper and lower soil elements, respectively, and σ_{FL} and σ_{FR} are tensile (compressive) stresses of the left and right soil elements, respectively, which can be expressed as:

$$\tau_{\text{down}} - \tau_{\text{up}} = \left(G \frac{\partial u}{\partial z} + G \frac{\partial^2 u}{\partial z^2} \right) - G \frac{\partial u}{\partial z} = G \frac{\partial^2 u}{\partial z^2} \tag{7}$$

$$\sigma_{\text{FL}} - \sigma_{\text{FR}} = \left(E \frac{\partial u}{\partial x} - E \frac{\partial^2 u}{\partial x^2} \right) - E \frac{\partial u}{\partial x} = E \frac{\partial^2 u}{\partial x^2} \tag{8}$$

where u is the horizontal displacement, G is the shear modulus, E is the elastic modulus, and z and x are the vertical and horizontal coordinates, respectively. Therefore, the dynamic equation of the soil elements in the slope can be expressed as follows:

$$\rho \frac{\partial^2 u}{\partial t^2} - G \frac{\partial^2 u}{\partial z^2} - E \frac{\partial^2 u}{\partial x^2} = \rho \frac{\partial^2 u_g}{\partial t^2} \tag{9}$$

Considering the viscous damping force, formula 9 can be expressed as follows:

$$\rho \frac{\partial^2 u}{\partial t^2} - G \frac{\partial^2 u}{\partial z^2} - E \frac{\partial^2 u}{\partial x^2} + c \frac{\partial u}{\partial t} = \rho \frac{\partial^2 u_g}{\partial t^2} \tag{10}$$

where c is the damping of the soil.

As the elevation increases, the maximum principal stress σ_1 and the minimum principal stress σ_3 of the slope soil gradually decrease to zero at the slope top in static conditions. Near the slope surface, the maximum and minimum principal stress directions are significantly deflected. Specifically, the maximum principal stress direction is parallel to the slope surface. Under the dynamic force, due to the transient dynamic shear stress, the coupled static–dynamic stress subjects the soil to continuous tensile and shear effects. Under the action of small ground motion, the dynamic stress transmitted between the skeleton particles is low. In addition, the sum of the coupled static–dynamic effect between the solid medium and the passive adaptive adjustment of the water–gas medium is lower than the sliding resistance σ_0 between the soil particles (Xie and Feng 2006). Therefore, no residual deformation occurs in the soil mass. The slope shows

left–right swing in the test process, and the shoulder region with the strongest amplification effect of PGA has the largest swing.

5.2.3 Stage of residual deformation

With the increase in the ground motion, under the continuous tensile and shear action of the dynamic stress, the soil microstructure is gradually damaged, leading to residual deformation (Fig. 16c). Residual deformation occurs in immersed soil and is the largest at the top of the slope and shows vertical seismic subsidence macroscopically. Over 1/2 of the slope surface, there is also seismic subsidence of the soil, but the displacement direction of the soil on the slope surface is both vertical and along the slope direction. The seismic subsidence increases from the bottom to the top and reaches the maximum at the shoulder of the slope. As the ground motion intensity continues to increase, due to the lower strength of the moisturized soil and the dynamic amplification effect in the slope, the dry–wet interface with sharp changes in wave impedance will produce strong tensile and shear stress, which aggravates the soil residual deformation in 1/2 the area of the slope and drastically reduces the soil strength. In addition, due to the low confining pressure characteristics of the slope top and slope surface, the local transient dynamic stress would exceed the tensile resistance of the soil, thereby resulting in tensile failure at the slope top and in 1/2 the area of the slope surface. The crack extension direction of the slope top is vertical to the horizontal direction, and the generation of tension cracks is mainly caused by horizontal dynamic stress σ_d . Under the action of ground motion, the maximum dynamic principal stress σ_{d1} on the slope surface is determined by the horizontal dynamic stress σ_d and the maximum principal stress σ_1 (static force), which can be expressed by the following formula:

$$\vec{\sigma}_{d1} = \vec{\sigma}_d + \vec{\sigma}_1 \quad (11)$$

Formula 11 shows that the size and direction of σ_{d1} are determined by σ_d and σ_1 . During the reciprocating action of σ_d , when the direction of σ_d inclines to the outside of the slope and the amplitude reaches a certain extent, cracks form in the slope surface, and the extension direction of the cracks is vertical to σ_{d1} . After cracks occur, water moves deep under the action of vibration, which provides convenience for water infiltration and immerses the deeper soil, and the mechanical strength becomes weak.

5.2.4 Sliding stage

With the continuous action of ground motion, the seismic subsidence of the soil on the upper slope increased further, and the cracks continued to expand deeper. Because the residual strength of the soil in the upper part of the slope becomes very low after seismic subsidence, under the continuous action of the ground motion, the low confining pressure state of the slope surface and the strong horizontal transient dynamic stress reciprocating action cause the surface soil divided by cracks to slide downward, the sliding range of the slope is from the area above 1/2 of the slope surface to the deepest crack at the top of the slope, and sliding displacement decreases gradually from the surface to inside (Fig. 16d). Macroscopic phenomena show that the slope sliding under dynamic action is that the surface soil drags the inner soil down, there is no uniform sliding surface in the sliding body, the wetted soil particles of the slope surface slip each other, and the sliding surface is the deepest to the crack tip.

From the above-mentioned staging process of the loess landslide, we can see that the modes and mechanism of loess landslides induced by the coupling of earthquakes and rainfall under different rainfall conditions are significantly different. The loess landslides induced by the coupling of earthquakes and continuous rainfall for many days are caused by liquefaction and slip of the soil mass (Sassa et al. 2007; Wang et al. 2017a, 2019, b). The landslides induced by the coupling of earthquakes and rainfall (light rain or moderate rain) are caused by seismic subsidence of the superficial soil mass of the slope.

6 Calculation method of the critical instability acceleration

In the shaking table model test of the slope, the critical instability acceleration of the slope is generally set as the basis for the slope stability evaluation. Because there is a difference between each working condition in the step-by-step loading of the shaking table test, the critical instability acceleration cannot be directly obtained. Therefore, the author intends to obtain accurate critical acceleration by the following method.

Based on the macroscopic failure characteristics, soil pressure, pore pressure of the low-angle slope model after rains and the variation in the peak value of the first-order natural frequency of the TFS curve (Fig. 5), it can be determined that the deformation and failure of the model soil mainly occurs in the middle and upper parts of the slope, while the deformation failure characteristics of the slope shoulder are prominent due to the large decrease in the peak of the TFS curve and the distortion of the curve adjacent to the peak in the local instability case (435 gal). In the instability case (647 gal), the TFS curve shows a fluctuating pattern with no prominent peak. According to the macroscopic failure and the change in the TFS curve, the critical instability acceleration of the slope is between 435 gal and 647 gal. From the peak of the TFS curve with the change in the ground motion, it is predicted that the peak (A_{cr}) of the TFS curve of the critical instability case should be greater than the maximum (A_{647}) of the TFS curve in the 647 gal case and lower than the peak (A_{435}) of the TFS curve in the 435 gal case, so:

$$A_{435} < A_{cr} < A_{647} \quad (12)$$

From the relationship between the peak of the TFS curve and the ground motion loading, the following formula can be obtained through fitting (Fig. 5):

$$A_{TFS} = -0.000005PGA^2 - 0.0087PGA + 10.939 \quad (13)$$

where A_i is the peak of the TFS curve at the A5 point in grade i case and PGA is the peak acceleration in each case. The critical instability acceleration value of the slope model can be accurately determined by the above formula, which should be between 435 gal and 458 gal. If the average value is taken, the critical instability acceleration A_{cr} is 446.5 gal.

7 Discussion and conclusions

1. After rainfall, the mechanical strength of the wetted soil in the certain surface layer of the loess slope is reduced. If the slope is subjected to moderate or strong earthquakes, in the process of transmission of seismic waves in the form of stress waves from the bottom to the top, due to the amplification effect of the ground motion, the middle and upper parts of the slope are subjected to strong tension, compression and shear action,

resulting in microstructural damage, seismic subsidence of the soil and a large number of cracks, and all of these enhance water infiltration and deep penetration of soil water. Under the action of subsequent ground motion, cracks extend to the deeper part, and seismic subsidence continuously increases. Finally, under the combined action of gravity and dynamic force, the upper soil mass in the seismic subsidence area drags the lower soil mass in the seismic subsidence area downward because of the sliding force being greater than the residual strength of the soil mass, which induces the seismic subsidence-type loess landslide. Under the coupling effect of earthquakes and rainfall, the instability mode and mechanism of this landslide are significantly different from that of the liquefaction type of landslide.

2. The loess landslide of seismic subsidence under the coupling effect of earthquakes and rainfall has the following three characteristics: (1) the landslide occurs in the superficial soil mass at the upper part of slope; (2) the surface soil mass drags the inner soil mass down, and every layer of soil slides downward from the outside to the inside, but the displacement decreases gradually from the outside to the inside; and (3) the deepest sliding plane is to the tip of the cracks.
3. Although the soil properties at different parts of the loess slope are basically the same, their vibration characteristics (natural frequency) are different. During the bottom-to-top transmission of earthquake waves, some frequency components close to the natural frequency are amplified, resulting in strong transient responses and increasing the amplification effect of the ground motion. As the dynamic load increases, the damage accumulation and the change in the mechanical properties of the soil and the vibration state of the slope system are changed, leading to the attenuation of the amplification effect. This indicates that the dynamic response of slopes will have temporal and spatial variability.
4. All the scientific studies start from the phenomenon to the essence. The failure of the slope model in this test is very similar to the failure phenomenon in the Yongdeng Ms5.8 earthquake in 1995, which indicates that the shaking table test method has certain advantages in reflecting the dynamic response characteristics of the slope and revealing the failure mechanism. However, reasonable instability criterion and certain calculation methods should be adopted to evaluate the seismic stability of the slope using the critical instability acceleration. The calculation method provided in this paper can produce more accurate results.


Acknowledgements This work is supported by Special Fund for Basic Scientific Research of Institute of Earthquake Prediction, China Earthquake Administration (No. 2018IESLZ07), Gansu Science and Technology Project (No. 18YF1FA101) and the National Natural Science Foundation of China (No. 51578518). The authors would like to express their gratitude to Professor Zhenming Wang for their helpful advice.

References

- Chen Y, Shi Y (2006) Basic characteristics of seismic landslides in the loess region of Northwest China. *Seism Stud* 03:276–280
- Deng L, Fan W (2013) Deformation and failure characteristics and development mechanism of loess landslide induced by Haiyuan M8.5 earthquake in Ningxia. *Disaster Sci* 03:30–37
- Deng J, Wang L, Zhang Z et al (2013) The china loess microstructure types and its seismic subsidence zones divided. *China Earthq Eng Geomechan J* 35(3):664–670 (in Chinese)
- Faris F, Fawu W (2014) Investigation of the initiation mechanism of an earthquake-induced landslide during rainfall: a case study of the Tandikat landslide, West Sumatra, Indonesia. *Geoenviron Disasters* 1:1–4

- Gao G (1994) The formation of collapsible properties of loess in China. *J Nanjing Univ Archit Eng* 2:1–8 (in Chinese)
- Jiang L, Yao L, Wu W, Xu G (2010) Application of transfer function analysis on slope shaking table model test. *Rock Soil Mech* 05:1368–1374
- Lin G, Zhu T, Lin B (2000) Similar techniques for structural dynamic model test. *J Dalian Univ Technol* 01:1–8
- Luan M, Li S, Yang Q (2006) Study on matrix suction and tension suction of unsaturated soils. *J Geotech Eng* 07:863–868
- Mein RG, Larson CL (1973) Modeling infiltration during a steady rain. *Water Resour Res* 9(2):384–394
- Qi J, Zhao G, Zhang Z, Wang L (1998) Characteristics and mechanism analysis of loess earthquake damage in the Yongde M5.8 earthquake in Gansu Province. *Northwest Seismol J* 01:71–76
- Sassa K, Wang G, Fukuoka H et al (2004) Landslide risk evaluation and hazard mapping for rapid and long-travel landslides in urban development areas. *Landslides* 1(3):221–235
- Sassa K, Fukuoka H, Wang F et al (2007) Landslides induced by a combined effect of earthquake and rainfall. *Progress of landslide*. In: Wang W, Sassa F (eds) *Progress in landslide science*. Springer, Berlin, pp 193–207
- Sassa K, Nagai O, Solidum R et al (2010) An integrated model simulating the initiation and motion of earthquake and rain induced rapid landslides and its application to the 2006 Leyte landslide. *Landslides* 7(3):219–236
- Wang L (2003) *Loess dynamics*, 1st edn. Earthquake Press, Beijing
- Wang L, Sun J (2014) Earthquake safety in town construction on the loess plateau. *Earthq Eng Eng Vib* 34(04):115–122
- Wang L, Pu X, Wu Z et al (2017a) The shaking table test of the instability sliding of loess slope under the coupling effects of earthquake and rainfall. *Chin J Rock Mech Eng* 36(S2):3873–3883
- Wang L, Wu Z, Xia K (2017b) Effects of site conditions on earthquake ground motion and their applications in seismic design in loess region. *J Mt Sci* 14(6):1185–1193
- Wang L, Pu X, Wu Z et al (2018) The shaking table test study on dynamic response of loess slope under earthquake and rainfall coupling. *Chin J Geotech Eng* 40(07):1287–1293
- Wang G, Ren L, Wu W et al (2019a) Characteristics and causes of the landslide outbreaking in Yongguangcun, Inxian County, Gansu Province. *J Glaciol Geocryol* 41(2):392–399
- Wang L, Che A, Wang L (2019b) Disaster characteristics and enlightenment of Hokkaido M6.7 earthquake. *City Disaster Reduct* 01:1–8
- Wu Z, Wang L, Chen T et al (2012) Study on the magnifying mechanism of earthquake ground in the far field loess site of Wenchuan earthquake. *Rock Soil Mech* 33(12):3736–3740
- Wu Z, Chen Y, Wang Q et al (2019) Disaster-causing mechanism of Yongguang landslide under Minxian-Zhangxian Ms6.6 earthquake. *Chin J Geotech Eng* 41(S2):165–168
- Xie D, Feng Z (2006) Some basic ideas on the study of effective stress in unsaturated soils. *Geotech Eng* 02:170–173
- Xu S, Wu Z, Sun J et al (2013) Study of the characteristics and inducing mechanism of typical earthquake landslides of the Minxian-Zhangxian MS6.6 earthquake. *China Earthq Eng J* 35(3):471–476
- Yuan Z, Wang L, Yan G (2012) Experimental study on loess water characteristic curve. *Eng Surv* 40(05):10–14
- Zhang Z (1999) *Earthquake disaster prediction of loess*. Earthquake Press, Beijing
- Zhang C, Li P, Li TL et al (2014) In-situ observation on rainfall infiltration in loess. *Shuili Xuebao* 45(6):728–734

Affiliations

Xiaowu Pu^{1,2}  · Lanmin Wang^{1,2} · Ping Wang^{1,2} · Shaofeng Chai^{1,2}

✉ Xiaowu Pu
wdpuxw@163.com

¹ Key Laboratory of Loess Earthquake Engineering of China Earthquake Administration, Lanzhou Institute of Seismology, CEA, Lanzhou 730000, Gansu, China

² Geotechnical Disaster Prevention Engineering Technology Research Center of Gansu Province, Lanzhou 730000, Gansu, China